A Highly Efficient, Scalable, Tetra-Band Metamaterial-Based Ambient RF Energy Harvester

Aaron M. Graham, *Graduate Student Member, IEEE*, Spyridon Nektarios Daskalakis, *Senior Member, IEEE*, Vincent Fusco, *Life Fellow, IEEE*, Manos M. Tentzeris, *Fellow, IEEE*, and Stylianos D. Asimonis, *Senior Member, IEEE*

***Abstract*—This article presents an innovative metamaterial-based radio frequency (RF) energy harvesting system designed to efficiently capture ambient RF energy across multiple frequency bands, including Wi-Fi (2.45 GHz) and 5G (0.9, 1.8, 2.1 GHz). Utilizing electric inductive-capacitive resonators and a rectification circuit, the system converts ambient RF energy into direct current (dc) power with high efficiency. Specifically, a single unit cell of the proposed 8 $\times$ 8 harvester is capable of generating up to 562 μW under an RF ambient power density of 40 μW/cm^2. This high efficiency and scalability make it ideal for powering low-power Internet-of-Things (IoT) devices and sensors. The design emphasizes optimizing the unit cell to minimize computational complexity, enabling a more straightforward and scalable implementation. Experimental results demonstrate the system's ability to efficiently harvest RF power across the specified bands, validating its potential as a sustainable solution for the growing power demands of IoT networks.**

***Index Terms*—Metamaterials, metasurfaces, radio frequency (RF) energy harvesting, rectifiers.**

I. Introduction

THE world is becoming increasingly connected through the deployment of wireless sensor networks (WSNs). The exponential rise of the Internet of Things (IoT) has brought unprecedented levels of autonomy and monitoring. In 2023, it was estimated that there were 16.7 billion IoT devices, with that number expected to increase to 29.7 billion devices by 2027 [1]. However, the scalability of current WSNs is being called into question. With billions more sensor nodes expected to be deployed worldwide, the sustainability of powering these nodes with batteries or mains supply is questionable. Maintaining and replacing batteries for a vast number of sensors will become unsustainable.

To address this challenge, efforts have been made to reduce the power consumption of sensor nodes and explore alternative methods of supplying the power required. One promising approach is radio frequency (RF) energy harvesting, particularly through wireless power transfer (WPT) and the harvesting of RF energy from ambient sources. WPT has been a significant focus of research in recent decades. WPT has the advantage of enabling wireless charging, although it requires constant excitation from a dedicated source to provide power to the end device. Thus, there has also been a strong focus on research related to harvesting RF energy from ambient sources, exploiting the proliferation of mobile communications and terrestrial transmission networks. These networks emit signals at various power levels and frequencies, providing an abundance of untapped electromagnetic (EM) energy. The integration of RF energy harvesting into IoT is vital for its long-term future, as the supply of energy needed for the sensors is one of the greatest barriers to IoT [2].

However, a limitation in integrating RF energy harvesting into IoT is the relatively low available ambient power density, which determines the sensitivity of RF harvesters.

The expected ambient RF power is expected to be approximately 40 μW/cm^2 [3], [4]. To fully exploit the RF energy available in the environment, harvesting systems should be ultra-sensitive and power-efficient. Additionally, these systems should be wideband to cover multiple frequency bands, as different environments may have varying frequency spectrums.

Conventionally, *rectenna* designs (i.e., antennas connected to RF-to-dc rectifiers) have been used to enable RF energy harvesting. Researchers have conducted extensive studies to improve the RF-to-dc conversion efficiency of rectification systems. Attention has been focused on achieving higher RF-to-dc efficiencies (over 25%) at lower input powers, such as below -10 dBm [5], [6], [7], [8], [9], [10]. Various approaches have been explored, including co-designed antenna and rectification circuit designs [11], [12], [13], wideband/multiband rectifiers, and compact rectifier designs [14], [15], [16], [17], [18]. These rectifiers have shown promising results, achieving high RF-to-dc efficiency for different frequency bands and input power levels. For example, in [16], a six-band dual circularly polarized (CP) rectenna for ambient RF energy harvesting is

Received 30 January 2025; revised 10 March 2025; accepted 12 March 2025. This work was supported by the Department of the Economy (DfE) in Northern Ireland as part of the Postgraduate Studentships Programme with Queen's University Belfast. The work of Stylianos D. Asimonis was supported by the Program "MEDICUS" of the University of Patras, Greece. *(Corresponding author: Aaron M. Graham.)*

Aaron M. Graham and Vincent Fusco are with the Institute of Electronics, Communications and Information Technology, Queen's University Belfast, BT3 9DT Belfast, U.K. (e-mail: agraham63@qub.ac.uk; v.fusco@ecit.qub.ac.uk).

Spyridon Nektarios Daskalakis is with the School of Engineering and Physical Sciences, Heriot-Watt University, EH14 4AS Edinburgh, U.K. (e-mail: daskalakispiros@gmail.com).

Manos M. Tentzeris is with School of Electrical and Computer Engineering, Georgia Institute of Technology, Atlanta, GA 30332 USA (e-mail: etentze@ece.gatech.edu).

Stylianos D. Asimonis is with the Department of Electrical and Computer Engineering, University of Patras, 26504 Patras, Greece (e-mail: s.asimonis@upatras.gr).

Digital Object Identifier 10.1109/TMTT.2025.3555848

presented. In the outdoor measurements, the average received power in the frequency bands of interest was found to be around −11.4 dBm, and the maximum harvested dc power was 8 μW, resulting in a total system's efficiency of 11% for −11.4 dBm power input.

However, rectennas usually need to be formed into rectenna grids/arrays to increase the delivered dc power to a load for a given ambient power density [19]. This adds complexity to the design and implementation of rectenna-based RF energy harvesting systems. On the other hand, there is increased interest in the field of RF energy harvesting using metamaterial-based structures [20], called metamaterial harvesters (MHs).

MHs are a type of metamaterial absorber (MA) [21], where the captured EM power is delivered to an RF-to-dc rectification system rather than dissipating to the metallic and/or dielectric parts of the structure, as is mainly the case with a typical MA. A typical RF MH includes two main components: the RF front-end part, which absorbs and channels the incident EM waves, and the rectification system, which receives the RF power and delivers dc power to the endpoint.

Designing an end-to-end MH system to achieve high overall rad-to-dc efficiency (i.e., the ratio of the dc output power delivered to the load to the incident power) with low power input remains challenging, particularly for multiband operation. Table I shows the state-of-the-art in regard to MH systems. It is clear that typical solutions operate at a single harvesting band.

In [22], an MH was proposed featuring miniaturized rectifiers to harvest 2.45 GHz. The design achieved a rad-to-dc efficiency of 44.5% at an incident power of 25 dBm. In [23], a series of nongridded patch unit cells were designed to target circular polarized waves at 24 GHz. This approach attained a rad-to-dc efficiency of 63% for 15.2 dBm. Work in [24] focused on making an easily scalable RF feed network to supply a single rectifier at the end of each branch. This method achieved 61% rad-to-dc efficiency for an input of 15 dBm at 2.2 GHz. In [25], an ERR unit cell and RF summation network were proposed. Supplying the RF power to a single rectifier, the system achieved a rad-to-dc efficiency of 40% for 12 dBm at 2.82 GHz. With a focus on electric-field-coupled (ELC) resonators, in [26], an MH was designed for 2.45 GHz and multiple polarization angles. The proposed structure achieved a rad-to-dc efficiency of 70%. In [27], ELC resonators were used to feed individual voltage doubling rectifiers. This design was able to achieve 76.8% rad-to-dc efficiency for an input power of 0.4 dBm. The work in [28] is a dual-band and wide-angle MH capable of harvesting 58% of the incident RF power at 0 dBm, using a uniplanar compact photonic bandgap (UC-PBG) design. The work in [29] used an array of patches to harness energy from 2.45 GHz. With their design, they were able to harvest 67% of the incident 2.45 GHz at 0 dBm. In [30], a cut-wire resonator was designed to feed a rectifying diode in the center of the I-shaped trace. At an incident power of −0.46 dBm, the MH achieved a rad-to-dc conversion efficiency of 27.7%. In [31], a cross-dipole MH operating at 3 GHz was designed. By placing diodes into the gaps of the unit cells, the MH achieved a rad-to-dc efficiency of 74% at −1.48 dBm incident power per unit cell. In [32], the proposed ELC resonator was able to harvest 55% of the target frequency at −2 dBm. Utilizing a split-ring resonator (SRR) MH, in [33], a rectifying diode was directly placed onto the unit-cell feed. This method achieved a rad-to-dc efficiency of 81% at 1.9 GHz, with an incident power of −5 dBm. The loaded gridded square loop (GSL) proposed in [34] shows how loaded square loops combined with a diode network can harvest 15.9% of the incident power at −6 dBm.

TABLE I

STATE-OF-THE-ART METAHARVESTERS FOR RF ENERGY HARVESTING

Work	unit-cell Dimension ($\lambda \times \lambda$) Array Size	Targeted Frequency (GHz)	Power Density (per band, mW/cm^2)	Incident Power (per band, dBm)	Maximum rad-to-dc Efficiency (%)
[22]	0.164×0.164 6×6	2.45	5	25*	44.5%
[23]	0.24×0.24 13 elements †	24	0.49*	15.2	63%
[24]	0.47×0.47 5×6	2.45	0.264	15	61%
[25]	0.147×0.147 8×8	3	0.114*	12	40%
[26]	0.136×0.136 12×12	2.4	0.172*	9	70%
[27]	0.197×0.197 1×5	2.45	0.19*	0.4	76.8%
[28]	0.258×0.258 4×4	2.4, 5	0.42*	0	58% @ 2.4 GHz 51% @ 5.8 GHz
[29]	0.11×0.11 4×4	2.45	0.03*	0	67%
[30]	0.5×0.5 16×16	2.18	0.1	−0.46	27.7%
[31]	0.175×0.175 7×7	3	0.178	−1.48*	74%
[32]	0.064×0.064 8×8	2.72	0.0175*	−2	51%
[33]	0.167×0.167 8×8	1.9	0.0126*	−5	81%
[34]	0.267×0.267 5×5	3.2	0.012*	−6	15.9%
This Work	0.1×0.1 8×8	0.9 1.8 2.1 2.45	0.58	8	44% @ 0.9 GHz 49% @ 1.8 GHz 43% @ 2.1 GHz 38% @ 2.45 GHz
			0.092	0	37% @ 0.9 GHz 42% @ 1.8 GHz 37% @ 2.1 GHz 31% @ 2.45 GHz
			0.0073	−11	19% @ 0.9 GHz 21% @ 1.8 GHz 18.5% @ 2.1 GHz 12.5% @ 2.45 GHz

† Arranged in a diagonally orientated grid array, consisting of 13 elements.
* Calculated values from work.

This work presents the design and experimental validation of a novel MH, which is multiband and highly efficient for low power input and power density, compared to the state-of-the-art as shown in Table I. Exploiting the highly efficient power delivery method of using an MA, more than 85% of the RF incident power is channeled successfully to the input of the rectifier in multiple 5G frequency bands, n1 (2.1 GHz), n2 (1.9 GHz), n3 (1.8 GHz), n8 (0.9 GHz) as defined in 5G New

RF Range 1 (NR FR1) [35] and Wi-Fi (2.45 GHz). To ensure meaningful levels of power are harvested, a highly efficient multiband rectification system was designed consisting of four branches, i.e., one per operating band.

This work introduces a novel rectifier design featuring a parallel branch configuration, where each rectifier branch operates independently. Unlike the conventional cascaded branch approach, which connects branches sequentially and suffers from efficiency losses when certain frequency tones are absent, the parallel configuration prevents inactive branches from drawing current or introducing diode losses. By allowing each branch to be optimized for its specific frequency and to function independently, the proposed design significantly reduces biasing losses and enhances system efficiency. This innovation makes the rectifier more resilient and efficient in environments with inconsistent or variable ambient RF signals.

The proposed MH system is capable of harvesting 562 μW (measured value) per unit cell across the four bands of interest for a power density of 40 μW/cm^2. The 8×8 array delivers a dc 39.1 mW (simulated value) at the same power density, utilizing dc combiner architecture and a different optimum load. The latter is close to the predicted 36 mW, assuming a lossless connection at the dc part. These findings are crucial for the design approach of MH systems because it allows the focus to be on the unit cell, significantly simplifying the computational effort. Additionally, based on Table I, it is evident that the proposed multiband (0.9, 1.8, 2.1, and 2.45 GHz) MH outperforms the existing state-of-the-art. Thus, the presented work introduces a novel tetra-band MH that integrates both EM absorbing and RF rectification functionalities. Unlike previous multiband MHs, which typically address single or dual-band operations and often lack integrated rectification functionality, this research combines tetra-band operation with an efficient RF-to-dc rectification process. To the best of our knowledge, this is the first end-to-end tetra-band MH system presented, offering a highly efficient solution for multiband RF energy harvesting.

II. MH RF Front-End

The RF front-end of the MH is characterized by its rad-to-RF efficiency, which is defined as the ratio of the RF power delivered to the rectifier, P_{RF}, to the incident RF power, P_{rad}. This can be mathematically expressed as follows:

$$\eta_{\mathrm{RF}} = \frac{P_{\mathrm{RF}}}{P_{\mathrm{rad}}}. \tag{1}$$

The configuration of the MH RF front-end can take various forms, with designs commonly categorized into SRRs [22], [33], ELCs [26], [27], [32], or patch unit cells [23], [24], [29]. Other configurations, such as cut-wire resonators [30], crossed dipoles [31], UC-PBG structures [28], and GSL designs [34], are less common compared to the aforementioned types. In the past decade, numerous studies have focused on designing MH RF front-ends with high rad-to-RF efficiency. For instance, in [36], a triple-band MH RF front-end was proposed, demonstrating rad-to-RF efficiencies of 94% at 0.9 GHz, 81% at 1.8 GHz, and 87% at 2.45 GHz. Similarly, Almoneef and Ramahi [37] introduced a compact and highly efficient MH RF front-end operating at 3 GHz, which achieved a measured rad-to-RF efficiency of 93%. In [38], the MH RF front-end attained a rad-to-RF efficiency of 84.4% at 2.45 GHz. Moreover, Ghaderi et al. [39] presented a polarization-insensitive and wide-angle MH RF front-end, achieving a maximum rad-to-RF efficiency of 95%. Additionally, Ghaderi et al. [40] introduced a dual-band MH RF front-end operating at 2.45 and 6 GHz, with a rad-to-RF efficiency exceeding 80%.

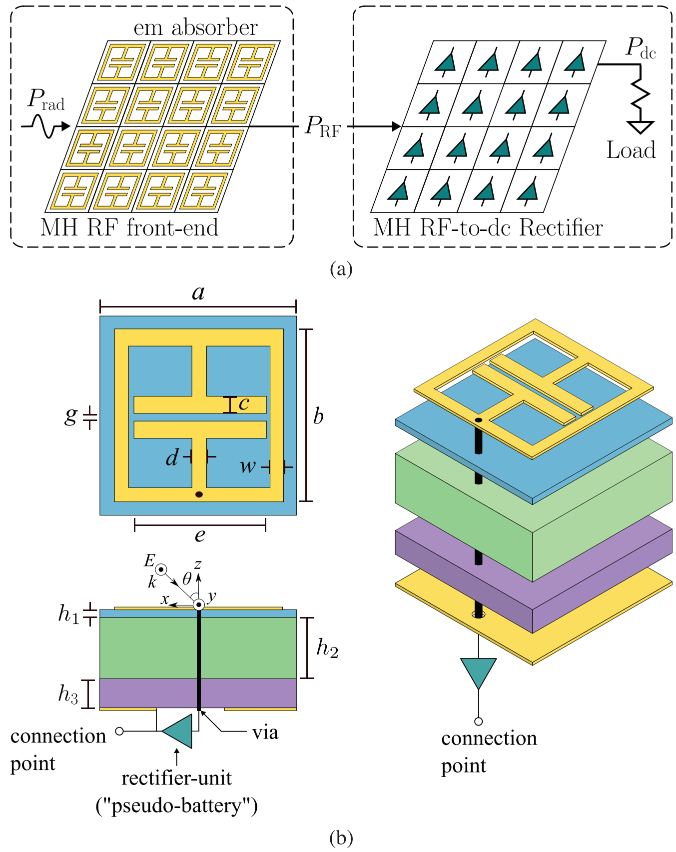

Fig. 1. (a) Schematic representation of the MH. The unit-cell geometry used for designing the proposed MH RF front-end structure (b): top view and side view (left), and a 3-D representation (right).

Fig. 1 shows the design of the unit cell from which the MH RF front-end is comprised. It comprises an ELC resonator, formed by a copper trace with a thickness of 35 μm and a conductivity of 5.8×10^7 S/m. ELC resonators offer several advantages over other electric resonator designs, including strong electric field coupling, design flexibility, compact size, and wideband performance [41]. These characteristics make them highly efficient and well-suited for applications such as metamaterial-based RF energy harvesters. This resonator is loaded with a resistor connected through a via, serving as the input impedance to a rectification system.

The design features a multilayer structure consisting of three different layers. The top layer is a Rogers RO4350B substrate, with a thickness of $h_1 = 0.51$ mm, a relative permittivity of $\varepsilon_r = 3.48$, and a loss tangent $\tan\delta = 0.0037$. The top layer hosts the copper trace to create the ELC resonator. The middle layer is a combination of an air gap and a 3-D printed lattice structure used to support the MH and the vias. The thickness

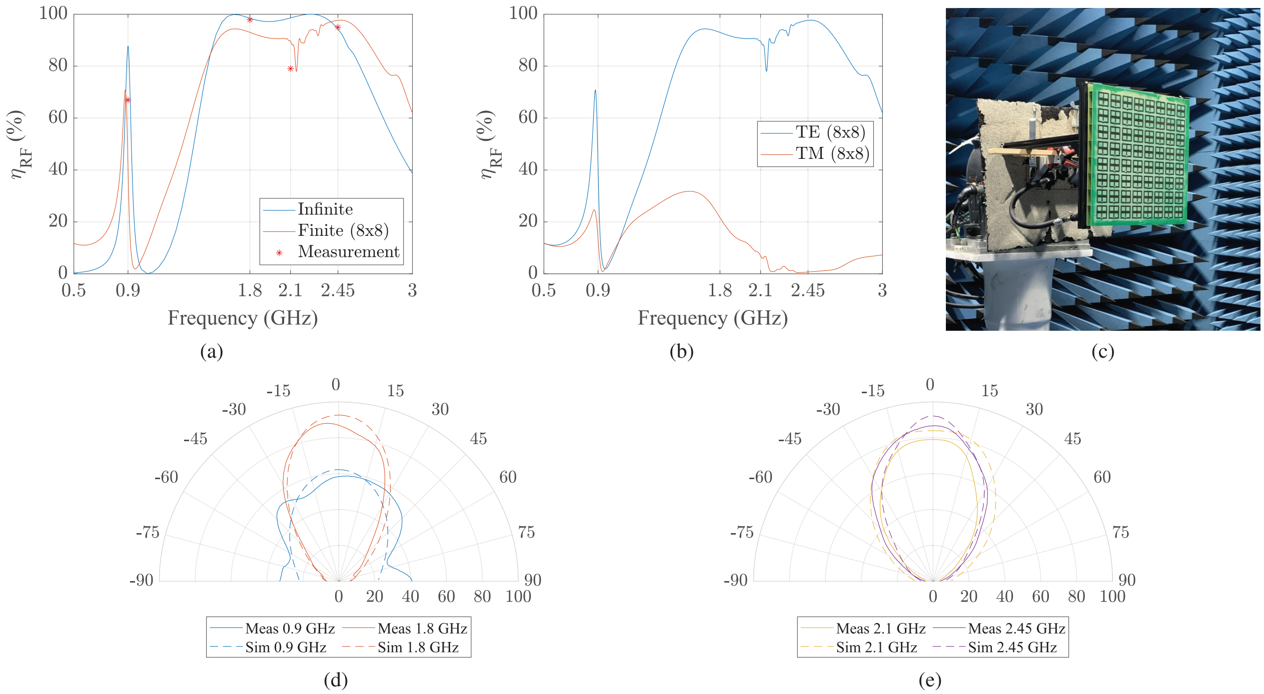

Fig. 2. (a) Comparison of simulated and measured rad-to-RF conversion efficiency η_{RF} for infinite and finite geometries across the operating frequency. (b) Simulated η_{RF} for TE and TM polarizations of the incident wave, demonstrating linear TE polarization. (c) Image of the fabricated MH RF front-end geometry used for experimental validation at 0.9, 1.8, 2.1, and 2.45 GHz. (d) and (e) Simulated and measured η_{RF} versus angle of incidence at specific frequency points for the finite 8×8 MH front-end geometry.

of the middle layer is $h_2 = 12$ mm. The material used in the 3-D printing is polylactic acid (PLA), with a relative permittivity of $\varepsilon_r = 2.72$. The bottom layer is an FR-4 substrate with a thickness of $h_3 = 1.6$ mm, a relative permittivity of $\varepsilon_r = 4.6$, and a loss tangent of $\tan\delta = 0.002$. This layered configuration results in a total thickness of 14.11 mm, which corresponds to approximately 0.042λ of the MH profile at 0.9 GHz. The RF front-end absorbs the incident RF energy and channels it to a load through a via. This via, with a diameter of 0.8 mm, runs between the top and bottom layers of the geometry and is connected to a 50-Ω load. This load mimics the input resistance of an RF-to-dc rectifier, which is then connected to the ground plane on the back of the bottom layer.

The design parameters were obtained through an optimization process using a genetic algorithm in CST Microwave Studio [42]. All simulations were conducted with the same software, employing the finite element method. The periodicity of the geometry was modeled by applying periodic boundary conditions (PBCs) around the unit-cell geometry, which was illuminated by a plane wave. The wave impinged on the structure either normally or at an angle, with a specific polarization. Specifically, the *unit-cell* option was used in the CST solver, corresponding to a Floquet boundary condition with a periodic port.

Considering a normally incident plane wave propagating along the z-direction with its electric field polarized in the y-axis, the design parameters for optimal η_{RF} were obtained at 0.9, 1.8, 2.1, and 2.45 GHz. The degrees of freedom for the optimization were the ELC parameters b, c, d, w, e, and g. The optimization process accounted for all these frequency points simultaneously. To enable the MH's front-end periodic structure to function as a homogeneous metamaterial-based EM absorber, the unit cell is fixed at a size of $a = 33.04$ mm, corresponding to approximately one-tenth of the maximum operating wavelength at 0.9 GHz. Utilizing this process, a multiband absorbing MH RF front-end structure was designed, and the dimensions of the ELC resonator are $b = 27.5$ mm, $c = d = w = 2.07$ mm, $e = 22.69$ mm, and $g = 0.39$ mm.

The entire structure can be characterized at its lower operating frequency (i.e., 0.9 GHz) as electrically thin, as it has an approximate thickness of $\lambda/23$, where λ is the wavelength at 0.9 GHz.

The simulated efficiency η_{RF} based on the unit-cell analysis using periodic conditions (i.e., infinite geometry) is depicted in Fig. 2(a). For normal incidence, two distinct highly absorbing regions appear: a narrow frequency band from 0.88 to 0.92 GHz and the other wideband from 1.48 to 2.61 GHz. In these regions, $\eta_{RF} \geq 80\%$ is achieved, resulting in a full-width half-maximum (FWHM) values of 6.8% and 69.9%, respectively. Specifically, at 0.9, 1.8, 2.1, and 2.45 GHz, the RF front-end achieves rad-to-RF efficiencies of 87.7%, 98.5%, 98.6%, and 94.3%, respectively.

When investigating metasurfaces, the common practice is to simulate the unit cell under the assumption of infinite periodicity. This approach simplifies the simulation and provides a good approximation of the behavior of the metasurface in an ideal, infinite scenario. However, when fabricating and measuring finite geometries, the actual physical structure includes edges and boundaries that can introduce edge effects and diffractive phenomena not accounted for in the unit-cell simulations [43]. These edge effects can lead to discrepancies between the simulated and measured results, as the interactions at the boundaries can significantly impact the overall performance and behavior of the metasurface. Therefore, considering these effects is crucial for accurately predicting and understanding the performance of practical, finite metasurface geometries. For this reason, we simulated the finite MH RF front-end with 8×8 unit cells, which was then fabricated and measured. The comparison between the simulated results of the infinite and finite MH RF front-end is depicted in Fig. 2(a). The difference between the results of the infinite and finite MH RF front-end is expected and mainly due to the edge effects as explained above.

The proposed metamaterial-based RF front-end is optimized for linear polarization under TE waves, as depicted in Fig. 2(b). For comparison, simulations were also conducted for TM polarization, with the results presented alongside the TE case in Fig. 2(b).

Next, the MH RF front-end geometry was fabricated and validated through measurements at 0.9, 1.8, 2.1, and 2.45 GHz within an anechoic chamber. The fabricated MH front-end can be seen in Fig. 2(c). For the measurement procedure, each unit cell was terminated with a load of 50 Ω through an SMA connector. By placing SMA connectors at each unit cell, between the corresponding ELC and rectifier, we gain the ability to measure the harvested RF power from each ELC, allowing us to estimate η_{RF}. Additionally, this setup enables regulation of the power input to the rectifier, facilitating the estimation of η_{dc}. In the final MH system, these SMA connectors will be removed.

The experimental conditions for measuring the RF power density, S, in this study were established by positioning the MH RF front-end, characterized by a physical surface area A_{rad}, at a fixed distance of $d = 5.35$ m from the transmitting source. The source was a horn antenna with a known gain, G_t [44], connected to a signal generator capable of delivering adjustable power levels, P_t, over a range of frequencies. On the receiving side, each unit cell of the RF front-end was individually connected to a spectrum analyzer to capture the received power, while the remaining unit cells were terminated with 50 Ω loads. This procedure was repeated 64 times for each frequency band. The total received power, P_{RF}, was determined as the sum of these individual measurements.

Using the Friis transmission equation for free-space propagation, the total received power is given by

$$P_{\mathrm{RF}} = P_t G_t \frac{A_r}{4\pi d^2} \tag{2}$$

where A_r represents the effective area of the MH RF front-end. Considering that $\eta_{\mathrm{RF}} = A_r / A_{\mathrm{rad}}$ [45] and (1), and substituting into (2), the radiated power can be expressed as

$$P_{\mathrm{rad}} = P_t G_t \frac{A_{\mathrm{rad}}}{4\pi d^2}. \tag{3}$$

Thus, by comparing the measured P_{RF} with the estimated P_{rad} from (3), the RF efficiency, η_{RF}, can be calculated. Comparing the simulated and measured η_{RF} between the infinite and finite cases [Fig. 2(a)], a good agreement between the results is observed.

Specifically, for the finite case, the simulated η_{RF} was 70.8%, 93%, 89.6%, and 97.7% at 0.9, 1.8, 2.1, and 2.45 GHz, respectively. In the infinite case, the simulated η_{RF} was 87.7%, 98.4%, 98.6%, and 94.3% at the same frequencies. The fabricated MH front-end, when measured, obtained an η_{RF} of 67%, 97.8%, 79%, and 95%. These results indicate a good agreement across the simulated structures and the fabricated MH front-end. The largest discrepancy occurs between the infinite and finite simulated cases at 0.9 GHz, where the wavelength is comparable to the geometry size, resulting in stronger edge effects, as expected.

Fig. 2(d) and (e) shows both the simulated and measured rad-to-RF conversion efficiency η_{RF} versus the angle of incidence at frequency points 0.9, 1.8, 2.1, and 2.45 GHz for the finite 8×8 MH front-end geometry. Specifically, in Fig. 2(d), at 0.9 GHz, the peak η_{RF} obtained in simulation was 62.3%, while the measured value fell to 58.9%. The location of the peak measured η_{RF} also shifted from 0° to 10°, which is an acceptable discrepancy due to fabrication imperfections and measurement misalignments. For 1.8 GHz, the simulated peak η_{RF} was 92.7% at $\theta = 0°$, with the measured value being 88.3% at $\theta = -8°$. Additionally, the η_{RF} remained greater than 80% for $|\theta| \leq 18°$ in simulation, which closely matches the fabricated MH front-end with $-18° \leq \theta \leq 14°$.

Fig. 2(e) shows the simulated and measured results for oblique incidence at 2.1 and 2.45 GHz. At 2.1 GHz, the measured peak η_{RF} is 79% compared to 83.9% in simulation, while at 2.45 GHz, the measured peak η_{RF} is 86.7% versus 92.2% in simulation. Additionally, at 2.45 GHz, the measurement shows an increased wide-angle response, staying above 80% η_{RF} for $-16° \leq \theta \leq 14°$ compared to $|\theta| \leq 14°$ in simulation.

Thus, the proposed MH RF front-end demonstrates high efficiency and wide-angle operation across multiple frequency bands, validating its potential for effective RF energy harvesting. The simulated and measured results for both infinite and finite geometries show good agreement, especially at the higher frequencies, with rad-to-RF efficiencies reaching up to 98.6%. The finite 8×8 MH front-end, when fabricated and tested, achieved promising results, maintaining high efficiency and performance even under oblique incidence. The largest discrepancies observed were due to edge effects at lower frequencies, which are expected in practical implementations. Overall, the proposed MH RF front-end offers an efficient solution for the design of multiband MHs.

III. MH RF-to-Dc Rectifier

Designing a multiband rectifier is a challenging task that involves addressing several technical issues to achieve optimal performance. One of the primary challenges is maintaining high RF-to-dc conversion efficiency across multiple frequency bands. This efficiency, denoted as

$$\eta_{\mathrm{dc}} = \frac{P_{\mathrm{dc}}}{P_{\mathrm{RF}}} = \frac{V_{\mathrm{dc}}^2}{P_{\mathrm{RF}} R_{\mathrm{L}}} \tag{4}$$

is the ratio of dc output power to RF input power, where V_{dc} is the dc output voltage across the output load R_{L}. This requires the development of sophisticated impedance-matching networks that can minimize losses and ensure efficient energy transfer. Furthermore, the rectifier must be capable of handling variations in load and input power, which can significantly impact performance. Techniques such as resistance compression networks (RCNs) are used to minimize sensitivity to these variations [46]. Additionally, achieving efficient energy harvesting in each band requires not only precise impedance matching but also effective use of rectifying elements (diodes), whose operation is nonlinear and depends on frequency, input power, and load. Another significant challenge is the compact integration of circuit components while supporting multiple frequency bands. Specifically, using passive microwave circuits like stubs for impedance matching is impractical as it significantly increases the circuit's size. Therefore, lumped components are often used instead. However, this approach increases design complexity, as it relies on models provided by manufacturers, which are often incomplete regarding input power or operating frequency.

In our case, the rectifier was designed for multiband operation, comprising four distinct branches tailored to specific frequency bands: 0.9, 1.8, 2.1, and 2.45 GHz. Each branch includes a matching network, which is a bandpass filter, a double Schottky diode for full-wave rectification, and capacitors to smooth the output dc voltage. All four branches are connected to a single load, representing either an electrical device powered by the rectifier (e.g., a wireless sensor node impedance input) or a battery charged by it.

In conventional multiband rectifier designs, each frequency band is typically associated with a distinct stage, commonly referred to as a branch. According to the state-of-the-art [16], [17], [18], [47], rectifier branches are often connected in series (or sequentially), a configuration that enables the strongest signal (or tone) to bias the diodes for weaker signals. This cascaded arrangement can be advantageous when multiple tones are present simultaneously, as it enhances energy conversion by allowing stronger signals to assist weaker ones in turning on the diodes and overcoming their threshold voltages. However, a significant drawback of *cascaded branches* is their inefficiency when certain tones are absent (i.e., when not all frequency bands are present). In such cases, the inactive branches continue to draw current without contributing to rectification, introducing diode losses that diminish overall system efficiency. As the number of inactive branches increases, the system becomes less efficient due to energy wasted in nonfunctional branches.

In contrast, a novel feature of the rectifier design presented in this work is the use of a *parallel branches*' configuration, enabling each rectifier branch to operate independently. In this arrangement, the presence or absence of signals in one branch does not influence the operation of other branches. Each branch is optimized for its specific frequency, and nonfunctional branches do not interfere with the performance of the active ones. This significantly reduces biasing losses, as nonoperational branches do not drain power from the system. Consequently, parallel branches are more efficient in environments where not all frequency tones are consistently available. Hence, the presented system's performance is more resilient

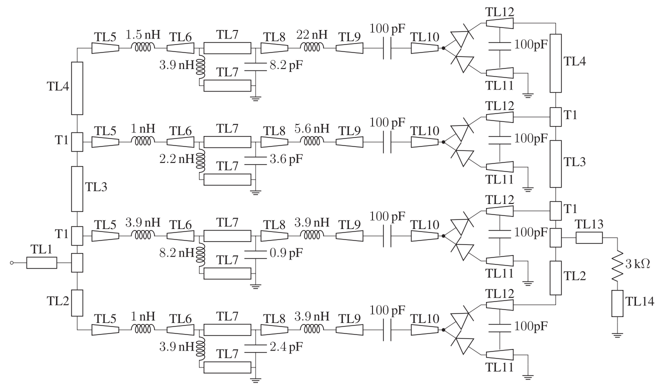

(a)

Microstrip	Length	Width (mm)	
Name	(mm)	Left	Right
TL1	12	1.35	–
TL2	3.5	1.35	–
TL3	5	1.35	–
TL4	10.05	1.35	–
TL5	3	1.35	0.85
TL6	2	0.85	1.35
TL7	2.45	1.35	–
TL8	2	1.35	0.85
TL9	3	0.85	1.3
TL10	3	1.35	0.5
TL11	3.8	0.5	1.35
TL12	7.7	0.5	1.35
TL13	3	0.9	–
TL14	1.95	0.9	–
T1	1.35	1.35	–

(b)

Fig. 3. (a) Finalized component values and circuit schematic of the tetra-band RF-to-dc rectifier unit, which is designed on an FR-4 substrate. The capacitors and inductors were sourced from Johanson Technology, and the diode used was the SMS7630-005LF Schottky diode from Skyworks. (b) Dimensions (mm) of the copper traces are also shown, with rectangular microstrips specified by two dimensions: length and width, while tapered strip lines are defined by three dimensions: length, left width, and right width.

to variations in ambient RF signals. Practically speaking, each branch is grounded individually, allowing a separate negative voltage feed line to enter each branch (Fig. 3). This differs from cascaded or serial designs, where a single ground via is often placed on the bottom branch, feeding both the bottom branch and each subsequent branch above it in the tree/circuit. This independent feed line enables each branch to bias its respective diodes independently, without passing through other branches. Additionally, the dc output of each branch is connected in parallel to the load impedance, unlike in cascaded designs, where the dc output is sequentially connected to each branch before finally reaching the load impedance.

A matching network similar to the one in [17] was used as the basis for the bandpass filter, as it demonstrated promising results in increasing bandwidth. The Skyworks Schottky Diode SMS7630-005LF was chosen for rectification due to its excellent performance under low input power levels typical of energy harvesting applications [48].

Using a typical voltage doubler, full-wave rectification is achieved with the capacitors placed before and after the diode arrangement, smoothing the obtained dc voltage [49]. The capacitors and inductors were sourced from Johanson Technology [50]. It is noted that it is crucial to carefully consider the operational limits of these components (inductors, capacitors, and diodes). The characteristics of lumped elements can vary significantly when operating outside their specified frequency ranges, which may adversely affect the overall performance of the system.

To keep the cost of the rectifier low, the circuit was designed on an FR-4 substrate with a thickness of 0.8 mm, a relative permittivity of 4.6, and a tangent loss of 0.002. The circuit was designed using Keysight ADS [51] solver, including lumped element parasitic losses in the design process.. The diode was modeled using the SPICE model provided by Skyworks in the datasheet, accounting for additional inductance and capacitance induced through soldering [52], [53]. The S-parameter models for the inductors and capacitors were provided from Johanson Technology, also modeled to include the extra solder capacitance.

To design the matching network circuit, a genetic algorithm was employed alongside harmonic balance (HB) analysis to obtain the maximum efficiency (η_{dc}) and the corresponding values of each capacitor and inductor component for optimal performance at each frequency. As part of the optimization process, a method for component selection was created in ADS, allowing the use of any manufacturer's S-parameter models. This approach enabled the design of the circuit based on measured data provided by the manufacturers, rather than ideal simulated models. To create an efficient optimization process, the branches were initially treated independently. Each branch targets a single frequency, so initially, each branch was considered an open circuit (o/c) from the rest. By opening the other three branches and optimizing a branch for a single frequency, the goal was to achieve a good match at the target frequency and allow the circuit to appear as an infinite impedance at the other frequencies. This ensures that each branch receives the maximum power for its respective frequency. However, once all branches are connected, the complex nature of the connection requires additional optimization to ensure each branch functions correctly. The optimization of the component values focused on η_{dc} at 0.9, 1.8, 2.1, and 2.45 GHz for an input power of −11 dBm. Hence, a multiobjective optimization was applied. It is noted again that to ensure compatibility with fabrication, the design process was limited to the commercial values for the capacitor and inductor components and their provided S-parameter models by the manufacturers, rather than a set of continuous values. The finalized component values, including the output load and the circuit schematic for the tetra-band RF-to-dc rectifier, are shown in Fig. 3. The optimum value for the output load varied with the operating frequency, ranging around 3000 Ω. The key variables affecting RF-to-dc efficiency are operation frequency, input power level, and output load impedance.

Thus, HB analysis was applied for these cases, as shown in Fig. 4. Initially, the input power P_{RF} was sequentially fixed at power levels of −6, −11, −16, and −21 dBm, and the frequency was varied within the range of 0.5–3 GHz. Additionally, the load was fixed at the optimum value of 3000 Ω, as explained. Fig. 4(b) depicts the results. It is evident that in both simulation and measurement that as the power level decreases, η_{dc} also decreases. Furthermore, η_{dc} is locally maximized at each of the four frequency points of interest. For example, for an input power of −6 dBm, the simulated η_{dc} is 47% at 0.9 GHz, 40% at 1.8 GHz, 39% at 2.1 GHz, and 28% at 2.45 GHz; for a −11 dBm power input, η_{dc} is 30%, 27%, 25%, and 14%, respectively.

Next, HB analysis was applied again to estimate η_{dc}, but this time the operating frequency was fixed at all four points of interest, with R_L = 3000 Ω. The RF power input ranged from −30 to 10 dBm. The η_{dc} was estimated and the results are plotted in Fig. 4(c). The best performance in terms of RF-to-dc rectification occurs at 0.9 GHz, while the lowest is at 2.45 GHz. It is evident again that as the input power increases, η_{dc} also increases. Note that beyond 5 dBm, the drop in efficiency is due to the diode model provided by the manufacturer, which is only valid up to this power level (this will also be corroborated by the measurements that follow). Following the same characteristic as Fig. 4(c), the output voltage is shown in Fig. 4(d). It can be seen again that as input power is increased the output voltage increases in line with that of the η_{dc}. However, above 5 dBm the voltage reaches a plateau which is the explanation for the drop in efficiency shown in Fig. 4(c). The impact of the output load on the RF-to-dc efficiency was also tested. The input power was fixed at −11 dBm, and HB analysis was applied at all four frequency points of interest while varying the output load impedance from 0.1 to 100 kΩ. The η_{dc} was calculated, and the results are depicted in Fig. 4(e). It can be observed that the maximum efficiency at each frequency band occurs very close to 3 kΩ, which is why R_L was set to this value throughout the simulations and measurements.

To experimentally validate the simulated results, a single rectifier unit was fabricated on a low-cost but lossy ($\tan\delta$ = 0.02) FR-4 substrate. The circuit was assembled using surface-mounted components (capacitors and inductors) from Johanson Technology, as mentioned. The rectifier's input was connected to an RF signal generator via a 50-Ω SMA connector. The output dc voltage was measured across a 3000-Ω load resistor using a digital voltmeter, allowing for the calculation of the η_{dc} based on (4) across various input power levels, ranging from −30 to 10 dBm, over a frequency span of 0.5–3 GHz. The digital voltmeter was programmed to sample the voltage at each interval, with a Python script controlling both the signal generator and the voltmeter to ensure precise synchronization between the devices throughout the testing process.

Initially, the RF power input P_{RF} was sequentially fixed at four different power levels: −6, −11, −16, and −21 dBm. The frequency was varied from 0.5 to 3 GHz, and the results are depicted in Fig. 4(b) by the dashed lines. For a −6 dBm power input, the measured (simulated) η_{dc} is 45% (47%), 33%

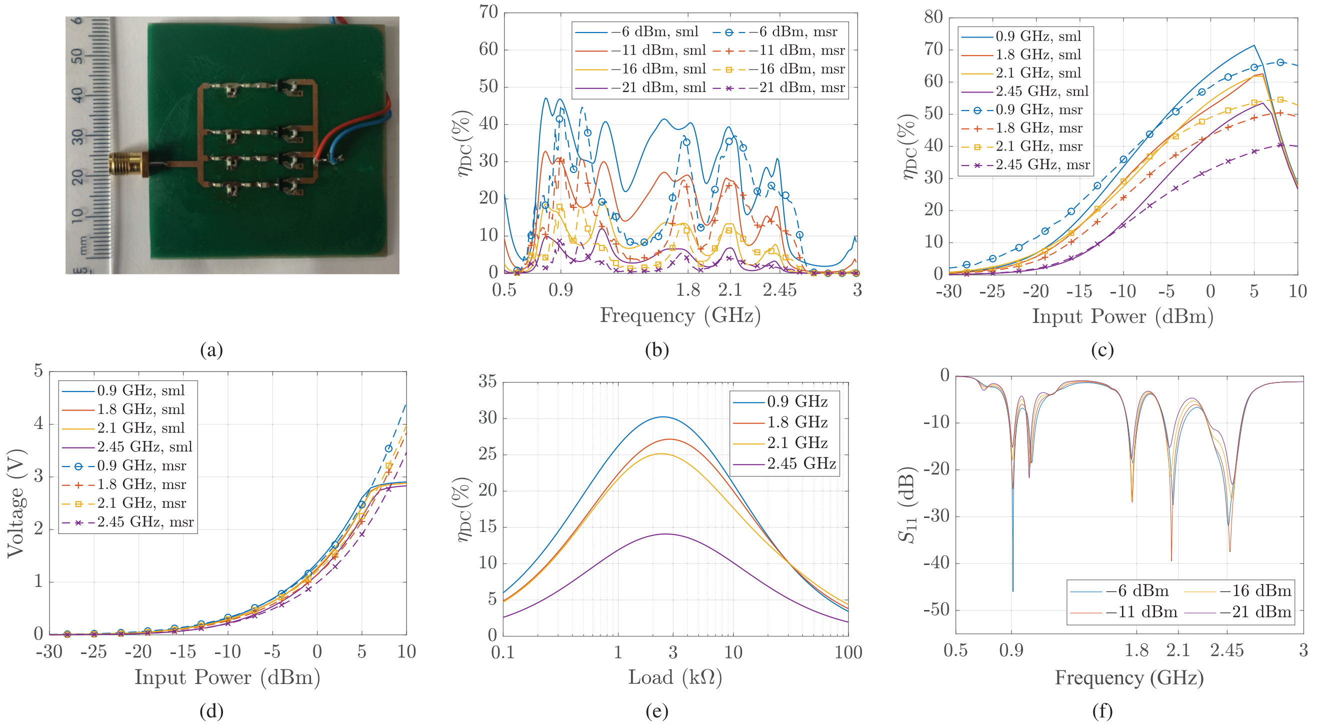

Fig. 4. (a) Image of the proposed rectifier is shown in sub-figure. The RF-to-dc efficiency, η_{dc}, of the proposed rectifier varies under different conditions. (b)-(f) Results for varying operating frequency, power input, and output load impedance, respectively. (b) Comparison of the simulated and measured η_{RF} for varying frequencies. With the η_{RF} under varying input power levels, for both simulated and measured shown in (c). The simulated and measured voltage for varied input power is presented in (d). (e) Simulated η_{RF} is shown when the load is swept from 100 to 100 k$/Omega$. The measured S_{11} of the proposed rectifier versus operating frequency is shown in (f). The close agreement between the experimental and simulated results validates the rectifier's performance across various conditions. Moreover, the rectifier achieves a maximum η_{dc} of 66%, maintaining efficiency above 40% for all four bands of interest at 8 dBm. For a low power input of −11 dBm, the measured η_{RF} ranges from 13% to 33% across the four bands.

(40%), 36% (39%), and 21% (28%) at 0.9, 1.8, 2.1, and 2.45 GHz, respectively. The agreement between the measured and simulated results is good, and the marginal discrepancy is mainly due to a slight shift in frequency in the measurements (e.g., at 1.78 GHz, measured $\eta_{dc} = 37\%$, closer to the simulated 40% at 1.8 GHz). For a lower power level of −11 dBm, where the circuit was optimized as mentioned, the measured (simulated) η_{dc} is 33% (30%), 22% (27%), 26% (25%), and 13% (14%), respectively.

Next, the frequency was sequentially fixed in the signal generator at all four bands of interest, while the power input was varied from −30 to 10 dBm. The results are depicted in Fig. 4(c) by the dashed lines. The 0.9-GHz band shows the highest RF-to-dc efficiency, ranging from 2% for −30 dBm up to 66% for 8 dBm power input. Similarly, the maximum measured η_{dc} at 1.8, 2.1, and 2.45 GHz occurs again for 8 dBm and is 50.5%, 54.5%, and 40.5%, respectively.

By comparing the simulated versus measured η_{dc} (i.e., Fig. 4(c), it is observed that the rectifier operates similarly at 1.8 and 2.1 GHz in the simulated results, but there is a difference in the measured results. This discrepancy is due to a slight offset in frequency in the measured geometry, as mentioned, and because the response at 1.8 GHz is more narrow-band, this shift has a higher impact on the η_{dc} for this band. Another observation is that the fabricated rectifier not only operates beyond 5 dBm power input but also presents its maximum RF-to-dc efficiency at 8 dBm, while in the simulated geometry, η_{dc} drops dramatically after 5 dBm. This is due to the provided models of the components used during the simulations, as mentioned. Fig. 4(d) shows the simulated and measured dc voltage output of the rectifier versus power input, respectively. The simulated voltage ranges from 0.2 to 2.9 V, while the measured voltage ranges from 0.2 to 3.5 V, as the power input increases from −11 to 8 dBm. In the simulated results, the plateau in voltage above 5 dBm occurs due to the diode models. Fig. 4(f) presents the measured reflection coefficient S_{11} versus frequency for various power input levels (−6, −11, −16, and −21 dBm). Based on the measurements, the rectifier demonstrates good impedance matching to 50 Ω, though a slight frequency shift of approximately 40 MHz is observed, particularly around 1.8 and 2.1 GHz.

Hence, the fabricated rectifier achieves a maximum RF-to-dc efficiency of 66%, maintaining efficiency levels above 40% across all four targeted bands at an input power of 8 dBm. For low power input levels of −11 dBm, the measured RF-to-dc efficiency ranges from 13% to 33% across the four frequency bands, demonstrating the rectifier's ability to operate efficiently even at low input power. This makes it highly suitable for multiband RF energy harvesting applications where ambient RF power levels are typically low.

IV. Metaharvester

Next, the developed MH RF front-end is integrated with the rectifier design to create a complete MH system. The

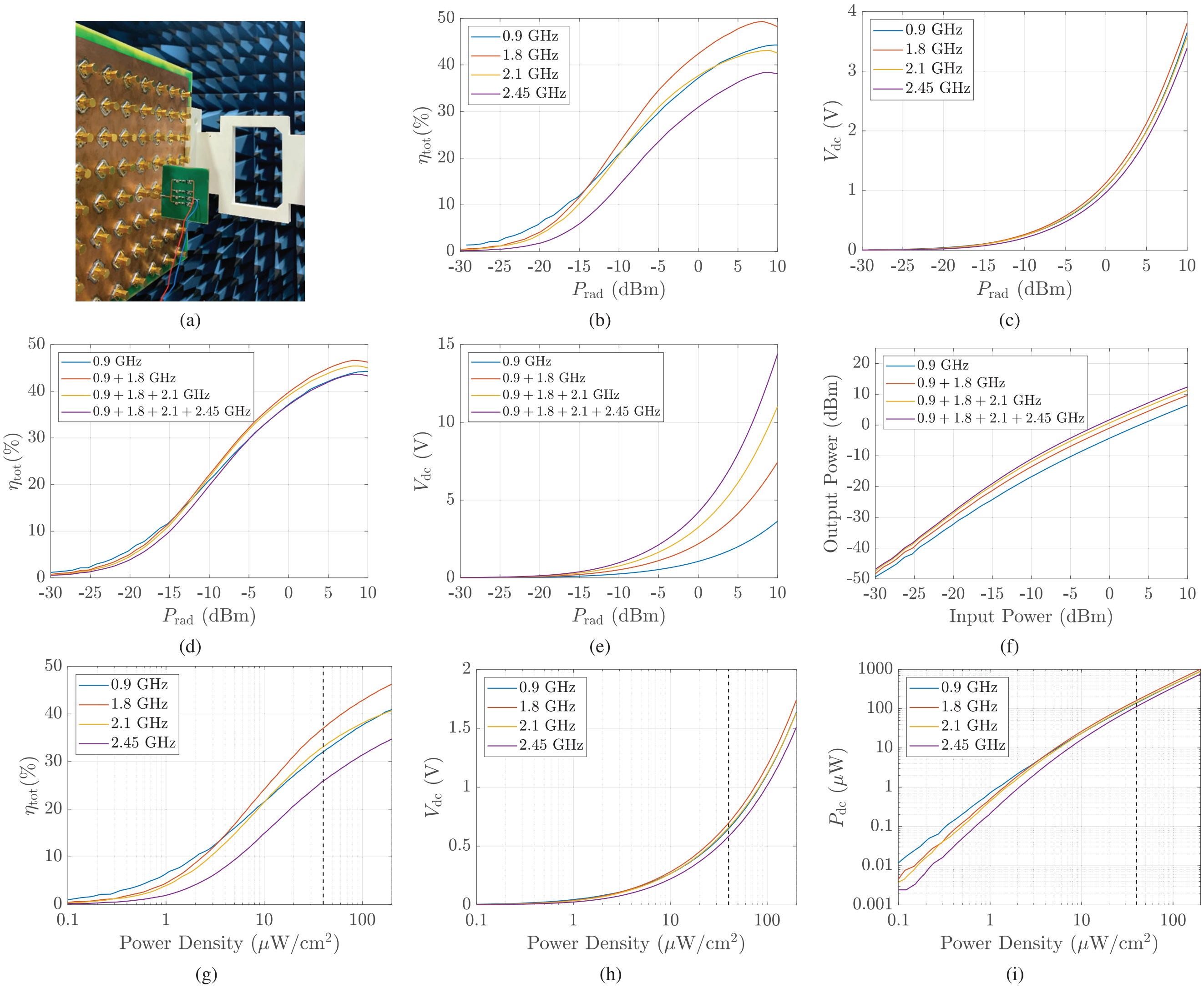

Fig. 5. Performance evaluation of the developed MH system. (a) Picture of the experimental setup used to measure the total efficiency, η_{tot}, where the rectifier is connected to one of the RF front-end's unit cells, and other unit cells are terminated with 50 Ω. (b) Measured η_{tot} versus P_{rad} at four different frequencies: 0.9 GHz, 1.8 GHz, 2.1 GHz, and 2.45 GHz. (c) Measured V_{dc} versus P_{rad} over the same frequency bands. (d) RF-to-dc efficiency versus P_{rad} for dual, triple, and tetra-band RF inputs, showcasing additive branch behavior. (e) Measured dc output voltage versus P_{rad} as the number of frequency bands increases. (f) Measured dc output power versus P_{rad}, demonstrating improved performance with additional frequency tones. (g) η_{tot} as a function of power density S, showing the performance at various environmental ambient RF power densities. (h) V_{dc} as a function of power density S. The black dashed lines in (d) and (e) represent the typical ambient RF power density level of 40 μW/cm^2. (i) Measured P_{dc} as a function of power density S for each of the four bands of interest. At a power density of 40 μW/cm^2, the MH delivers 141, 162, 145, and 114 μW at 0.9, 1.8, 2.1, and 2.45 GHz, respectively, resulting in a total harvested power of 562 μW per unit cell.

performance of this MH system is evaluated based on its ability to capture incident EM power per band (P_{rad}) and convert it to dc power (P_{dc}).

This conversion efficiency, referred to as the rad-to-dc efficiency, is mathematically defined as

$$\eta_{\mathrm{tot}} = \frac{P_{\mathrm{dc}}}{P_{\mathrm{rad}}} = \eta_{\mathrm{RF}}\,\eta_{\mathrm{dc}}. \tag{5}$$

One of the primary advantages of an MH over a conventional rectenna system is its scalability. An MH features a periodic geometry composed of small electrical unit-cell rectennas, which can be connected on the dc side, akin to the cells in a photovoltaic panel. Consequently, to consider this scalability, we chose to measure the total efficiency, η_{tot}, of the proposed MH by focusing on a single unit cell. To validate the performance of the MH, we connected the fabricated rectifier to one of the RF front-end's unit cells, as depicted in Fig. 5(a). All other unit cells were terminated with 50 Ω. We then conducted measurements similar to those used to estimate η_{RF}. The MH was positioned at a distance, d = 5.35 m, from the horn antenna, and the harvested dc power, P_{dc}, was measured using a voltmeter.

The measured η_{tot} versus P_{rad} is depicted in Fig. 5(b). For an incident power of 8 dBm, η_{tot} (harvested power) is 44% (2.8 mW), 49% (3.1 mW), 43% (2.7 mW), and 38% (2.4 mW) at 0.9, 1.8, 2.1, and 2.45 GHz, respectively. For a lower power of −11 dBm, η_{tot} (harvested power) across these four bands adjusts to 19% (15.3 μW), 21% (16.7 μW), 18.5% (14.7 μW), and 12.5% (9.8 μW), respectively. Hence, the MH is capable of harvesting P_{dc} = 56.5 μW for P_{rad} = −11 dBm, per unit cell and a maximum of P_{dc} = 11 mW for P_{rad} = 8 dBm. Table I also depicts the total efficiency of the MH for P_{rad} = 0 dBm, where the total harvested power reaches P_{dc} = 1.6 mW. Fig. 5(c) depicts the measured V_{dc} versus P_{rad}, where it is observed that the output dc voltage varies from 0.2 to 3 V as the P_{rad} increases from −11 to 8 dBm.

As previously discussed, the proposed design employs a parallel branch configuration within the rectifier circuit, enabling each branch to function independently and efficiently at its specific frequency. This approach contrasts with cascaded designs, where inactive branches may draw power and compromise overall efficiency. By isolating inactive branches, the parallel configuration mitigates biasing losses and ensures reliable performance, even when certain frequency tones are absent. The impact of the parallel branch configuration is also depicted in Fig. 5(d)–(f). The measured RF-to-dc efficiency versus P_{rad} for dual, triple, and tetra-band input RF signals is depicted in Fig. 5(d). The results confirm the additive behavior of the active rectifier branches, with the overall RF-to-dc efficiency remaining stable, ranging from 20% to 22% for $P_{\mathrm{rad}} = -20$ dBm as the number of tones increases, unaffected by the inactive branches. Additionally, as the number of bands increases, the rectified dc output voltage [Fig. 5(e)] and power [Fig. 5(f)] also increase. Specifically, the dc output power improves from −32.2 dBm for a single tone to −28 dBm for four tones at $P_{\mathrm{rad}} = -20$ dBm. These findings underscore the robustness of the proposed parallel configuration design approach.

Also, P_{rad} was converted into power density S using the following formula:

$$S = \frac{P_{\mathrm{rad}}}{A_{\mathrm{rad}}}. \quad (6)$$

A comparative analysis of spot or long-term RF EMF measurements in the EU revealed that the mean electric field strengths ranged between 0.08 and 1.8 V/m. In some instances, these strengths could escalate to as much as 20 V/m. Under the assumption of a plane wave, these values equate to power densities of up to 106 μW/cm^2 [54]. Additionally, based on the works [3] and [4], although they mention that the ambient RF power density varies depending on the environment, they cite a typical power density of RF ambient energy as 40 μW/cm^2. The measured results, namely, η_{tot} and V_{dc}, as functions of S, are depicted in Fig. 5(g) and (h), respectively. In these figures, the black dashed line represents the anticipated power level in the ambient environment, up to 40 μW/cm^2. It is clear that the MH can operate from a power density as low as 0.1 μW/cm^2. As the power density escalates, both η_{tot} and V_{dc} increase correspondingly. Specifically, at a power density of 40 μW/cm^2, the minimum η_{tot} of 26% is observed at 2.45 GHz, while the maximum η_{tot} of 37% is observed at 1.8 GHz. Similarly, V_{dc} equals 0.6 V at 2.45 GHz and 0.7 V at 1.8 GHz for the same power density, while for the other two bands of interest, it lies between these two values.

Fig. 5(i) presents the measured P_{dc}, which is the dc power harvested from a single unit cell, as a function of S. It is evident that, given a power density of 40 μW/cm^2 for each of the four bands of interest (0.9, 1.8, 2.1, and 2.45 GHz), the MH delivers 141, 162, 145, and 114 μW, respectively. Consequently, a total power of 562 μW can be harvested by a single unit cell at a power density of 40 μW/cm^2 across these four bands of interest.

In this work, a dc combiner network is chosen rather than an RF combiner network [3], as mentioned. The dc combiner network offers several benefits, including a simplified system design by aggregating the rectified outputs from each unit cell into a single output, requiring only one resistive load or storage unit. This setup provides a design that is generally easier and less complex compared to an RF combiner network, particularly when integrating multiple unit cells, thus enhancing scalability. In contrast, RF combiners can reduce the power density required per unit cell to activate a single rectification circuit by constructively combining the RF contributions from each cell. However, designing an RF combiner network that ensures the effective combination of RF power from multiple unit cells into a single rectification circuit is more complex, especially for dual-band or multiband systems, such as the proposed MH. Consequently, increasing the number of unit cells can make the design of the RF combiner extremely difficult, rendering it less suitable for large-scale systems and diminishing scalability. Despite its advantages, the dc combiner network has its drawbacks. Each unit cell requires a rectifier diode, which leads to diode losses.

These losses can diminish system efficiency, particularly under low ambient power densities. For S = 40 μW/cm^2, the total harvested power from a single unit cell is 562 μW, summing up the contribution of each of the four bands of interest, as mentioned. Thus, theoretically, the fabricated 8 × 8 MH could deliver up to 36 mW, assuming a uniform power level present at each unit cell. To validate this value, we simulated the total P_{dc} of the 64 unit cells using the dc combiner architecture. In this setup, the dc output of each unit cell in a row is connected in series, with the ends connected to the other rows in parallel, and the single dc output is connected to a single output load. The total P_{dc}, harvested across the four bands of interest, is maximized as a function of load, with all other design parameters fixed, and for a power density of 40 μW/cm^2. It was found that for a load of 25 Ω, P_{dc} reaches 39.1 mW, breaking down to 9.2, 12.4, 9.5, and 8 mW at 0.9, 1.8, 2.1, and 2.45 GHz, respectively. This demonstrates that the total MH with the dc combiner architecture presents an optimum load different from the optimum for a single unit cell, as discussed in previous studies [10], [19]. Additionally, it is noted that as the number of combined unit cells increases, the optimum load decreases. Furthermore, our work found that the simulated total P_{dc} of 39.1 mW is very close to the estimation of 36 mW extrapolated from the measurement of the single unit cell, assuming a uniform power level is absorbed in each unit cell and not considering the edge effects of the finite MH geometry. Also, please note that in the simulated geometry, the rectifiers connected to each unit cell use a separated ground plane to mimic the measurements [Fig. 5(a)]. This finding first shows that dc combination leads to marginal connection losses. Additionally, this finding is crucial in the design approach of MH systems because it allows the focus to remain on the unit cell, significantly simplifying the computational effort. Consequently, scalability mainly affects the value of the output load and not the impedance-matching network or the design of the RF-to-dc rectifier circuit.

V. Discussion

In stark contrast to other state-of-the-art multiband RF harvesting systems [16], [18], [24], [55], [56], [57], [58], the proposed design demonstrates a notable scalability advantage. In conventional rectenna systems, scaling up often involves adding multiple antennas and rectifiers, leading to increased complexity, potential RF signal combination losses, and interference. In contrast, our MH employs a periodic geometry that inherently supports scalability, enabling power output to increase simply by adding more unit cells to the structure. Each unit cell functions as an independent "pseudo-battery," converting RF energy directly into dc power, which is then combined through a dc combiner network. This modular approach allows for straightforward expansion without complex RF signal handling and maintains efficiency as more cells are added. Moreover, the combination of the metamaterial-based structure with a dc combiner network further distinguishes this work from conventional approaches. The dc combiner network simplifies the integration of multiple unit cells by directly aggregating the dc output of each cell, effectively supporting milli-Watt level energy harvesting without the complexity of RF signal combination. This approach allows the system to maintain high efficiency and scalability, making it a viable solution for the continuous low-power energy needs in IoT networks.

Another significant innovation of this design lies in the parallel configuration employed in the rectifier circuit, which markedly improves efficiency in low-power, multiband ambient environments. Traditional multiband rectifiers often connect branches in series (cascaded), where each branch can be activated by the strongest available signal to assist weaker signals in overcoming diode threshold voltages. However, this cascaded arrangement suffers from efficiency losses when certain frequency tones are absent, as inactive branches continue to draw current, leading to diode losses that reduce overall efficiency. In contrast, the proposed rectifier design uses a parallel configuration in which each branch operates independently and is optimized for its specific frequency band. This arrangement prevents inactive branches from drawing current, reducing biasing losses, and enabling the system to perform efficiently even when not all frequency tones are present. This parallel configuration makes the system more resilient to variations in the availability of the ambient RF signal.

VI. Conclusion

This study introduces a novel tetra-band MH system that integrates EM absorption and RF rectification functionalities, showcasing superior performance across multiple frequency bands, including 5G (0.9, 1.8, and 2.1 GHz) and Wi-Fi (2.45 GHz). The system achieves high efficiency, up to 98.6% for the RF front-end and between 13% and 66% for the rectifier, distinguishing it from current solutions. Scalability and a focus on unit-cell design simplify computational efforts. Experimental results validate the system's capability to harvest power across various frequency bands and power densities. For instance, the MH system harvests 562 μW per unit cell across the four bands, achieving a power density of 40 μW/cm^2. In an 8×8 array configuration using a dc combiner architecture, the total harvested power can reach 39.1 mW under the same power density condition, with the assumption the power delivered to each unit cell is uniform, maximizing the total dc power output of 64 unit cells as a function of load, while holding other design parameters constant. This research offers promising and scalable RF harvesting solutions for powering small electrical devices in the IoT era.

References

[1] S. Sinha, "State of IoT 2023: Number of connected IoT devices growing 16% to 16 billion globally," IoT Anal., Hamburg, Germany, Tech. Rep., Spring 2023. [Online]. Available: https://iot-analytics.com/number-connected-iot-devices/

[2] D. Evans, "The Internet of Things how the next evolution of the internet is changing everything," CISCO Internet Bus. Solutions Group (IBSG), San Jose, CA, USA, White Paper, Apr. 2011. [Online]. Available: https://iot-analytics.com/number-connected-iot-devices/

[3] F. Fatima, M. J. Akhtar, and O. M. Ramahi, "Frequency selective surface structures-based RF energy harvesting systems and applications: FSS-based RF energy harvesting systems," *IEEE Microw. Mag.*, vol. 25, no. 3, pp. 47–69, Mar. 2024.

[4] M. A. Ullah, R. Keshavarz, M. Abolhasan, J. Lipman, K. P. Esselle, and N. Shariati, "A review on antenna technologies for ambient RF energy harvesting and wireless power transfer: Designs, challenges and applications," *IEEE Access*, vol. 10, pp. 17231–17267, 2022.

[5] S. D. Assimonis and A. Bletsas, "Energy harvesting with a low-cost and high efficiency rectenna for low-power input," in *Proc. IEEE Radio Wireless Symp. (RWS)*, Jan. 2014, pp. 229–231.

[6] S. D. Assimonis, S.-N. Daskalakis, and A. Bletsas, "Efficient RF harvesting for low-power input with low-cost lossy substrate rectenna grid," in *Proc. IEEE RFID Technol. Appl. Conf. (RFID-TA)*, Sep. 2014, pp. 1–6.

[7] H. Shen, Y.-X. Guo, and Z. Zheng, "Design of a high-efficiency 2.45-GHz rectenna for low-input-power energy harvesting," *IEEE Antennas Wireless Propag. Lett.*, vol. 11, pp. 929–932, 2012.

[8] S. D. Assimonis, S.-N. Daskalakis, and A. Bletsas, "Sensitive and efficient RF harvesting supply for batteryless backscatter sensor networks," *IEEE Trans. Microw. Theory Techn.*, vol. 64, no. 4, pp. 1327–1338, Apr. 2016.

[9] S. D. Assimonis, V. Fusco, A. Georgiadis, and T. Samaras, "Efficient and sensitive electrically small rectenna for ultra-low power RF energy harvesting," *Sci. Rep.*, vol. 8, no. 1, p. 15038, Oct. 2018.

[10] S. D. Assimonis, S. N. Daskalakis, V. Fusco, M. M. Tentzeris, and A. Georgiadis, "High efficiency RF energy harvester for IoT embedded sensor nodes," in *Proc. IEEE Int. Symp. Antennas Propag. USNC-URSI Radio Sci. Meeting*, Jul. 2019, pp. 1161–1162.

[11] C. Song, Y. Huang, J. Zhou, J. Zhang, S. Yuan, and P. Carter, "A high-efficiency broadband rectenna for ambient wireless energy harvesting," *IEEE Trans. Antennas Propag.*, vol. 63, no. 8, pp. 3486–3495, Aug. 2015.

[12] V. Palazzi et al., "A novel ultra-lightweight multiband rectenna on paper for RF energy harvesting in the next generation LTE bands," *IEEE Trans. Microw. Theory Techn.*, vol. 66, no. 1, pp. 366–379, Jan. 2018.

[13] A. M. Graham and S. D. Asimonis, "Practical superdirective and efficient rectenna for low-power RF energy harvesting," in *Proc. IEEE-APS Top. Conf. Antennas Propag. Wireless Commun. (APWC)*, Sep. 2024, pp. 188–191.

[14] W. Liu, K. Huang, T. Wang, J. Hou, and Z. Zhang, "A compact high-efficiency RF rectifier with widen bandwidth," *IEEE Microw. Wireless Compon. Lett.*, vol. 32, no. 1, pp. 84–87, Jan. 2022.

[15] B. L. Pham and A.-V. Pham, "Triple bands antenna and high efficiency rectifier design for RF energy harvesting at 900, 1900 and 2400 MHz," in *IEEE MTT-S Int. Microw. Symp. Dig.*, Jun. 2013, pp. 1–3.

[16] C. Song et al., "A novel six-band dual CP rectenna using improved impedance matching technique for ambient RF energy harvesting," *IEEE Trans. Antennas Propag.*, vol. 64, no. 7, pp. 3160–3171, Jul. 2016.

[17] V. Kuhn, C. Lahuec, F. Seguin, and C. Person, "A multi-band stacked RF energy harvester with RF-to-DC efficiency up to 84%," *IEEE Trans. Microw. Theory Techn.*, vol. 63, no. 5, pp. 1768–1778, May 2015.

[18] A. N. Parks and J. R. Smith, "Sifting through the airwaves: Efficient and scalable multiband RF harvesting," in *Proc. IEEE Int. Conf. RFID (IEEE RFID)*, Apr. 2014, pp. 74–81.

[19] S. D. Assimonis and V. Fusco, "RF energy harvesting with dense rectenna-arrays using electrically small rectennas suitable for IoT 5G embedded sensor nodes," in *IEEE MTT-S Int. Microw. Symp. Dig.*, Aug. 2018, pp. 1–3.

[20] L. Li, X. Zhang, C. Song, and Y. Huang, "Progress, challenges, and perspective on metasurfaces for ambient radio frequency energy harvesting," *Appl. Phys. Lett.*, vol. 116, no. 6, Feb. 2020, Art. no. 060501.

[21] N. I. Landy, S. Sajuyigbe, J. J. Mock, D. R. Smith, and W. J. Padilla, "Perfect metamaterial absorber," *Phys. Rev. Lett.*, vol. 100, no. 20, May 2008, Art. no. 207402.

[22] X. Duan, X. Chen, and L. Zhou, "A metamaterial harvester with integrated rectifying functionality," in *Proc. IEEE/ACES Int. Conf. Wireless Inf. Technol. Syst. (ICWITS) Appl. Comput. Electromagn. (ACES)*, Mar. 2016, pp. 1–2.

[23] W. Huang, J. Du, X. Yang, W. Che, and S. Gao, "A novel 24 GHz circularly polarised metasurface rectenna," *IET Microw., Antennas Propag.*, vol. 17, no. 6, pp. 419–426, May 2023.

[24] F. Erkmen, T. S. Almoneef, and O. M. Ramahi, "Scalable electromagnetic energy harvesting using frequency-selective surfaces," *IEEE Trans. Microw. Theory Techn.*, vol. 66, no. 5, pp. 2433–2441, May 2018.

[25] M. El Badawe, T. S. Almoneef, and O. M. Ramahi, "A metasurface for conversion of electromagnetic radiation to DC," *AIP Adv.*, vol. 7, no. 3, Mar. 2017, Art. no. 035112.

[26] T. S. Almoneef, F. Erkmen, and O. M. Ramahi, "Harvesting the energy of multi-polarized electromagnetic waves," *Sci. Rep.*, vol. 7, no. 1, pp. 1–14, Nov. 2017.

[27] L. KangHyeok and S. K. Hong, "Rectifying metasurface with high efficiency at low power for 2.45 GHz band," *IEEE Antennas Wireless Propag. Lett.*, vol. 19, no. 12, pp. 2216–2220, Dec. 2020.

[28] L. Li, X. Zhang, C. Song, W. Zhang, T. Jia, and Y. Huang, "Compact dual-band, wide-angle, polarization- angle -independent rectifying metasurface for ambient energy harvesting and wireless power transfer," *IEEE Trans. Microw. Theory Techn.*, vol. 69, no. 3, pp. 1518–1528, Mar. 2021.

[29] W. Zhang, Y. Huang, and J. Zhou, "Wide-beam rectenna design using multi-port metasurface-based antenna," in *Proc. Int. Appl. Comput. Electromagn. Soc. (ACES-China) Symp.*, Jul. 2021, pp. 1–2.

[30] R. Wang et al., "Optimal matched rectifying surface for space solar power satellite applications," *IEEE Trans. Microw. Theory Techn.*, vol. 62, no. 4, pp. 1080–1089, Apr. 2014.

[31] A. Z. Ashoor and O. M. Ramahi, "Polarization-independent cross-dipole energy harvesting surface," *IEEE Trans. Microw. Theory Techn.*, vol. 67, no. 3, pp. 1130–1137, Mar. 2019.

[32] M. El Badawe and O. M. Ramahi, "Efficient metasurface rectenna for electromagnetic wireless power transfer and energy harvesting," *Prog. Electromagn. Res.*, vol. 161, pp. 35–40, 2018.

[33] M. A. Aldhaeebi and T. S. Almoneef, "Highly efficient planar metasurface rectenna," *IEEE Access*, vol. 8, pp. 214019–214029, 2020.

[34] S. Keyrouz, G. Perotto, and H. J. Visser, "Frequency selective surface for radio frequency energy harvesting applications," *IET Microw., Antennas Propag.*, vol. 8, no. 7, pp. 523–531, May 2014.

[35] R. Dilli, "Analysis of 5G wireless systems in FR1 and FR2 frequency bands," in *Proc. IEEE 2nd Int. Conf. Innov. Mech. Ind. Appl. (ICIMIA)*, Mar. 2020, pp. 767–772.

[36] S. D. Assimonis, T. Kollatou, D. Tsiamitros, D. Stimoniaris, T. Samaras, and J. N. Sahalos, "High efficiency and triple-band metamaterial electromagnetic energy hervester," in *Proc. 9th Int. Conf. Electr. Electron. Eng. (ELECO)*, Nov. 2015, pp. 320–323.

[37] T. S. Almoneef and O. M. Ramahi, "Metamaterial electromagnetic energy harvester with near unity efficiency," *Appl. Phys. Lett.*, vol. 106, no. 15, Apr. 2015, Art. no. 153902.

[38] W. Hu et al., "Low-cost air gap metasurface structure for high absorption efficiency energy harvesting," *Int. J. Antennas Propag.*, vol. 2019, pp. 1–8, Sep. 2019.

[39] B. Ghaderi, V. Nayyeri, M. Soleimani, and O. M. Ramahi, "Multi-polarisation electromagnetic energy harvesting with high efficiency," *IET Microw., Antennas Propag.*, vol. 12, no. 15, pp. 2271–2275, Dec. 2018.

[40] B. Ghaderi, V. Nayyeri, M. Soleimani, and O. M. Ramahi, "Pixelated metasurface for dual-band and multi-polarization electromagnetic energy harvesting," *Sci. Rep.*, vol. 8, no. 1, p. 13227, Sep. 2018.

[41] B. Thakur and A. Kunte, "Improved design of CELC meta-resonators for bandwidth improvement and miniaturization of patch antenna," *Appl. Phys. A, Solids Surf.*, vol. 124, no. 12, p. 860, Dec. 2018.

[42] D. Systèmes, *CST studio suite electromagnetic field simulation software*. Paris, France: Dassault Systèmes, Jun. 2023.

[43] D. R. Smith, D. C. Vier, T. Koschny, and C. M. Soukoulis, "Electromagnetic parameter retrieval from inhomogeneous metamaterials," *Phys. Rev. E, Stat. Phys. Plasmas Fluids Relat. Interdiscip. Top.*, vol. 71, no. 3, Mar. 2005, Art. no. 036617.

[44] *Drh-118 Horn Antenna*, Sunol Sciences Corporation, Dublin, CA, USA, Jul. 2024.

[45] C. A. Balanis, *Antenna Theory: Analysis and Design*. Hoboken, NJ, USA: Wiley, 2005.

[46] K. Niotaki, A. Georgiadis, A. Collado, and J. S. Vardakas, "Dual-band resistance compression networks for improved rectifier performance," *IEEE Trans. Microw. Theory Techn.*, vol. 62, no. 12, pp. 3512–3521, Dec. 2014.

[47] R. Keshavarz and N. Shariati, "Highly sensitive and compact quad-band ambient RF energy harvester," *IEEE Trans. Ind. Electron.*, vol. 69, no. 4, pp. 3609–3621, Apr. 2022.

[48] *Surface-Mount Mixer and Detector Schottky Diodes*, Skyworks, Irvine, CA, USA, Mar. 2021.

[49] S. N. Daskalakis, A. Georgiadis, A. Collado, and M. M. Tentzeris, "An UHF rectifier with 100% bandwidth based on a ladder LC impedance matching network," in *Proc. 12th Eur. Microw. Integr. Circuits Conf. (EuMIC)*, Georgia, Oct. 2017, pp. 411–414.

[50] *RF Ceramic Chip Inductors*, Johanson, Camarillo, CA, USA, May 2024.

[51] *PathWave Advanced Design System*, Keysight-Technologies, Santa Rosa, CA, USA, Oct. 2022.

[52] S.-Y. Tang, Q.-H. Xiao, T.-H. Song, and X.-C. Wei, "Influence of solder on de-embedded capacitance," in *Proc. Asia–Pacific Int. Symp. Electromagn. Compat. (APEMC)*, Sep. 2022, pp. 186–188.

[53] A. Alex-Amor, J. Moreno-Núñez, J. M. Fernández-González, P. Padilla, and J. Esteban, "Parasitics impact on the performance of rectifier circuits in sensing RF energy harvesting," *Sensors*, vol. 19, no. 22, p. 4939, 2019.

[54] P. Gajšek, P. Ravazzani, J. Wiart, J. Grellier, T. Samaras, and G. Thuróczy, "Electromagnetic field exposure assessment in Europe radiofrequency fields (10 MHz–6 GHz)," *J. Exposure Sci. Environ. Epidemiol.*, vol. 25, no. 1, pp. 37–44, Jan. 2015.

[55] Y.-S. Chen and J.-W. You, "A scalable and multidirectional rectenna system for RF energy harvesting," *IEEE Trans. Compon., Packag., Manuf. Technol.*, vol. 8, no. 12, pp. 2060–2072, Dec. 2018.

[56] S. Shen, Y. Zhang, C.-Y. Chiu, and R. Murch, "A triple-band high-gain multibeam ambient RF energy harvesting system utilizing hybrid combining," *IEEE Trans. Ind. Electron.*, vol. 67, no. 11, pp. 9215–9226, Nov. 2020.

[57] Y. Wei et al., "A multiband, polarization-controlled metasurface absorber for electromagnetic energy harvesting and wireless power transfer," *IEEE Trans. Microw. Theory Techn.*, vol. 70, no. 5, pp. 2861–2871, May 2022.

[58] S. Roy, R. J. Tiang, M. B. Roslee, T. Ahmed, and M. A. P. Mahmud, "Quad-band multiport rectenna for RF energy harvesting in ambient environment," *IEEE Access*, vol. 9, pp. 77464–77481, 2021.